Supplementary Materials

Calibration-free optical waveguide bending sensor for soft robots

Liang Zhong[1,#], Xiaoqing Tian[2,#], Ji-Yong Wang[3], Jian-Xiang Wang[1], Zhanguo Nie[1], Xueyin Chen[1], Yuxin Peng[1,*]

[1]Institute of Exercise Science and Health Engineering, Zhejiang University, Hangzhou 310058, Zhejiang, China.

[2]School of Mechanical Engineering, Hangzhou Dianzi University, Hangzhou 310018, Zhejiang, China.

[3]School of Electronic and Information, Hangzhou Dianzi University, Hangzhou 310018, Zhejiang, China.

[#]Authors contributed equally.

*Correspondence to: Prof. Yuxin Peng, Institute of Exercise Science and Health Engineering, Zhejiang University, Yuhangtang Road 866, Hangzhou 310058, Zhejiang, China, E-mail: yxpeng@zju.edu.cn

Supplementary Text 1. Manufacture procedure of the proposed sensor

Supplementary Figure 1a shows the section diagrams of the DCLS sensor, featuring a clear core measuring 150 mm (*L*) × 3.5 mm (*b*) × 3.5 mm (*t*) embedded within the proposed sensor, specifically sized at 150 mm (*L*) × 10 mm (*W*) × 10 mm (*H*). The clear core serves as the central element, flanked by sealed red and blue layers, each measuring 2 mm (*h*) × 3 mm (*a*) × 30 mm (*l*), meticulously positioned on opposing sides.

Supplementary Figure 1b and c illustrate the relationship between the LED luminous area size and the angle of incidence. Due to the refractive index limitations of the materials, the critical angle for total internal reflection is relatively large. To achieve total internal reflection within the light-guiding medium, it is necessary to minimize the angle of incidence as much as possible. According to Snell's law ($\theta_c = \arcsin\left(\frac{n_2}{n_1}\right)$ where n_2 and n_1 represent the refractive indices of the cladding and the clear core, respectively. θ_c is the critical angle), the critical angle is approximately 80°. In this study, the LED emission area used is larger than the cross-sectional area of the clear core, allowing for an incident angle θ_{i1} that is smaller than the critical angle, as shown in Figure 1b. However, LEDs with smaller emission areas have a larger beam angle, resulting in an incident angle θ_{i2} that is smaller than θ_{i1}, thereby leading to poorer total internal reflection performance (Figure 1c).

The detailed manufacturing process is illustrated in Supplementary Figure 2. We engineered modular 3D-printed molds specifically to facilitate the cladding layer of the DCLS sensor. Firstly, to form the bottom cladding layer, the EcoFlex 00-10 Part A and B were mixed in a 1:1 ratio and fully stirred. Then, the mixture was poured into a beaker and defoamed in a vacuum bucket. Following the removal of internal bubbles, the liquid silicone was poured into the lower 3D-printed mold. An upper 3D-printed mold fits together with it to complete the assembly, as depicted in Supplementary

Figure 2 (a and b). The entire ensemble underwent curing at 60°C for 3 hours on a heating platform (LICHEN, LC-DMS-H, China). Upon completion, the bottom cladding layer was detached from the assembly. Supplementary Figure 2 (c and d) shows the fabrication process of the red layer and the clear core. Clear liquid PDMS (Sylgard184, Dow Corning, USA) was mixed with the curing agent and the red colorant (SO-Strong, Smooth-On, USA) at the volume ratio of 600:100:1 to form red liquid PDMS, which was inked on the cavity of the cladding layer via an injector. Unlike the cladding layer curing, the red liquid PDMS required curing at 80°C for 12 hours on the heating platform. A mixture of 2.4 mL of clear liquid PDMS and 0.6 mL of curing agent was employed to coat the surface of the red layer and the cladding layer, solidifying at 80°C for 6 hours on the heating platform. Upon curing the clear core, we designed a specialized groove mold to fabricate the partial cladding layer and the cavity of the blue layer. By placing the groove mold on the bottom cladding layer, the positioning of the blue layer was secured. Liquid silicone was then applied to encapsulate the clear core, as shown in Supplementary Figure 2e. The fabrication process for the blue layer mirrored that of the red layer. After removing the groove mold, the cavity was filled with blue liquid PDMS ($V_{clear\ liquid\ PDMS} : V_{curing\ agent} : V_{red\ colorant} = 600 : 100 : 1$), as depicted in Supplementary Figure 2f. The semi-finished product was transferred to the heating platform and cured at 80°C for 12 hours. Finally, liquid silicone was inked to the surface of the blue layer to form an upper cladding layer [Supplementary Figure 2g]. Completing the construction involved cutting both ends of the sensor to expose the clear core, finalizing the main assembly of the DCLS sensor, as shown in Supplementary Figure 2h. The DCLS sensor utilizes substrate materials commonly found in traditional bending sensors. However, unlike these conventional sensors, the DCLS does not require additional sensing materials as its sensing element, thereby reducing material costs. Furthermore, this study introduces a manufacturing process based on mold casting, which simplifies the production of flexible sensors and makes it a universal and easily implementable method. This approach holds potential for large-scale industrial production.

Supplementary Text 2. Sensor circuit design

The optical signal was acquired using a chromatic detector. Specifically, the TCS3472 chromatic detector (ams AG, Austria) was employed for signal detection, integrated onto a customized printed circuit board (PCB) via surface mounted technology (SMT) process. An LED (5700k, Xlamp XQ-E, USA) connected to a 10 Ω current-limiting resistor was mounted at one end of the DCLS sensor (Supplementary Figure 6). Visible light within the wavelength spectrum of 350 nm to 770 nm was coupled to the clear core. Subsequently, the optical signal, captured by the chromatic detector, was transmitted to the microcontroller (STM32F103RCT6, STMicroelectronics, Italy) through the IIC bus. Then, the pre-processing data was transmitted to a personal computer (PC) for comprehensive analysis.

The LED and chromatic detector serve as the core components of the DCLS sensor, offering advantages such as compact size and low cost. Additionally, they can be produced on a large-scale using SMT, which presents significant prospects for industrial application.

Supplementary Text 3. Theoretical analysis

Intensity modulation stands as the prevailing method employed in optical sensors. Based on this method, this study undertakes a theoretical investigation into the working principle of the DCLS sensor. According to Planck's blackbody radiation theorem (1), the relative energy density at a fixed wavelength can be expressed as:

$$s(\lambda) = \frac{2\pi c^2 h}{\lambda^5} \cdot \frac{1}{e^{ch/k\lambda T} - 1} \tag{S1}$$

where λ, c, h, k, and T are wavelength, speed of light, Planck coefficient, Boltzmann constant, and blackbody temperature, respectively.

Let P_R and P_B represent the relative spectral power of the red and blue light, respectively. The P_R and P_B can be described as:

$$\begin{cases} P_R = \int_{760nm}^{620nm} s(\lambda)d\lambda \\ P_B = \int_{400nm}^{480nm} s(\lambda)\,d\lambda \end{cases} \tag{S2}$$

where $d\lambda$ is the differential wavelength. According to the Beer-Lambert Law ($A = ecl$) (2), the relationship between the absorbance of red and blue light and their relative spectral power in the initial state can be derived as follows:

$$\begin{bmatrix} A_R \\ A_B \end{bmatrix} = \begin{bmatrix} kP_R \\ kP_B \end{bmatrix} \tag{S3}$$

where k is the coefficient of calibration. When the sensor undergoes bending, differential stretching occurs on its upper and lower surfaces, inducing modifications in the optical paths of the red and blue layers. Consequently, the relative spectral power of the red light and blue light can now be denoted as $P_R{'}$ and $P_B{'}$, respectively. The change in absorbance can be described as:

$$\begin{bmatrix} \Delta A_R \\ \Delta A_B \end{bmatrix} = \begin{bmatrix} k(P_R - P_R{'}) \\ k(P_B - P_B{'}) \end{bmatrix} \tag{S4}$$

The relationship between the relative spectral power and the change of the light path can be obtained as follows:

$$\begin{bmatrix} \Delta l_R \\ \Delta l_B \end{bmatrix} = \begin{bmatrix} k(P_R - P_R')/ec \\ k(P_B - P_B')/ec \end{bmatrix} \tag{S5}$$

The stretching length of the red and blue layers can be expressed as Δl_R and Δl_B, respectively. Here, d signifies the distance between the center of the clear core and the upper and lower surfaces of the waveguide, while R represents the bending radius. The relationship between the bending angle and the stretching length can be expressed as:

$$\begin{bmatrix} \Delta l_R \\ \Delta l_B \end{bmatrix} = \begin{bmatrix} (R + 2d)\theta \\ (R + d)\theta \end{bmatrix} \tag{S6}$$

The equation S6 can also be expressed as:

$$\theta = \frac{\Delta l_R - \Delta l_B}{d} \tag{S7}$$

According to the equations S5 and S7, the bending angle can be obtained:

$$\theta = \frac{k(P_R - P_R') - k(P_B - P_B')}{ecd} = \frac{k}{ecd}(\Delta P_R - \Delta P_B) \tag{S8}$$

According to the above derivation, the DCLS sensor showcases the capability to disentangle the impact of the radius, thereby accommodating different curvature joints. It should be noted that a certain thickness of the sensor must be considered to allow for a deformation difference between the upper and lower surfaces of the sensor. This is necessary for accurately calculating the curvature and bending angle. Too small sensor thickness will affect its measurement accuracy. Therefore, during the size optimization, both the application scenario and measurement accuracy need to be considered simultaneously.

Moreover, discerning the direction of the bend is feasible through the disparity in light intensity. A positive or negative difference between red and blue light intensities respectively characterizes positive or negative bending.

Supplementary Text 4. Working principle of the non-stretchable and stretchable bending sensors

Supplementary Figure 7a depicts the operational mechanism of the non-stretchable bending sensor (3). To gain the sensor' signal, this sensor was connected in series with resistor R_0 to construct a complete bleeder circuit, which was powered by a stable voltage source (5 V). One end of the sensor and the series-connected resistor R_0 are connected to the data acquisition system (USB-1608G, National Instruments, USA) to capture the bending signal of the sensor. The output signal can be expressed as:

$$Signal = \frac{(\Delta R_t - \Delta R_{initial})}{R_{initial}} \tag{S9}$$

where $\Delta R_{initial}$ and ΔR_t indicate the resistance value of the sensor in its initial state and at time t, respectively.

Supplementary Figure 7b shows the working principle of a stretchable bending sensor (4), utilizing silicone as its flexible substrate and liquid metal as the sensitive material. The initial length of the liquid metal is denoted as L. Upon attachment to a human joint, the sensor undergoes overall elongation during bending, resulting in a total length increase to $L+\Delta L$. The resistance of the sensor can be expressed as:

$$R = \frac{\rho l}{s} \tag{S10}$$

where ρ is the conductivity of the liquid metal; l and s are the micro-channel length and cross-sectional area of the liquid metal, respectively. The liquid metal was filled into the sensor using a micro-channel injection method (5). Bending the sensor induces overall stretching, leading to an increase in resistance that facilitates the accurate mapping of the bending angle. The relationship between the bending angle and the output signal of the non-stretchable sensor was determined through linear fitting, as depicted in Supplementary Figure 7c. Following the same methodology, we also calibrated the stretchable sensor (Supplementary Figure 7d).

Supplementary Text 5. Characteristic comparisons of three types of bending sensors

To demonstrate the merits of the DCLS sensor, we conducted a comparative analysis involving both conventional non-stretchable and stretchable bending sensors.

Firstly, in order to compare the calibration-free characteristics of these sensors, we fabricated three sets of distinct joint protective equipment tailored to various sensor configurations. A participant followed instructions to wear the protective equipment (wrist guard, elbow pad and knee pad) to bend the wrist, elbow, and knee from a neutral state (0°) to a bending state (30°). When employing the non-stretchable sensor to measure the angles of these three joints, angular deviations of 5.2%, 22.8%, and 43.3% were observed respectively. The stretchable sensor, on the other hand, displayed angular deviations of less than 2.0% for the wrist, 33.3% for the elbow, and 183.3% for the knee. In contrast, during the evaluation of various joint flexion angles using the DCLS sensor, the disparity between its measurements and the established gold standard (indicated by the red dotted line) consistently remains below 2.0%. For the non-stretchable sensor, it was observed that larger joint areas result in smaller angle measurements. This phenomenon can be attributed to the inherent limited deformability of non-stretchable sensors when applied to larger joint areas. Conversely, the stretchable bending sensor exhibits an increasing tendency towards larger angular measurements as the joint bending radius increases. This correlation is due to a direct proportional relationship between the elongated arc length of the sensor and the radius associated with joint flexure ($L = \alpha R$, where L, α, and R are the arc length, bending angle, and radius, respectively). Remarkably, the DCLS sensor demonstrates outstanding calibration-free characteristic attributes across diverse joint configurations, further highlighting its robust performance in adapting to diverse bending conditions.

Secondly, to assess calibration-free bidirectional discernment, the participant executed wrist flexion and extension at a predetermined angle ($\alpha = 30°$) while wearing

safeguards equipped with different sensors. The results in Supplementary Figure 8a show the response signal of the non-stretchable sensor, where the magnitude and amplitude of the signal response remain consistent, resulting in an inability to differentiate between bending directions. Supplementary Figure 8b shows the response signal of the stretchable sensor during wrist flexion and extension. Remarkably, during wrist joint flexion, the sensor portrays a pronounced response, contrasting with a relatively minor response observed during wrist joint extension. This observed variance is attributed to the greater elongation experienced by the sensor affixed to the safeguards during wrist joint flexion movements. Upon flexion and extension of the wrist using the safeguard with the DCLS sensor, a normalized change rate of light intensity can be observed in the Supplementary Figure 8c, which can be utilized to determine the corresponding bending direction.
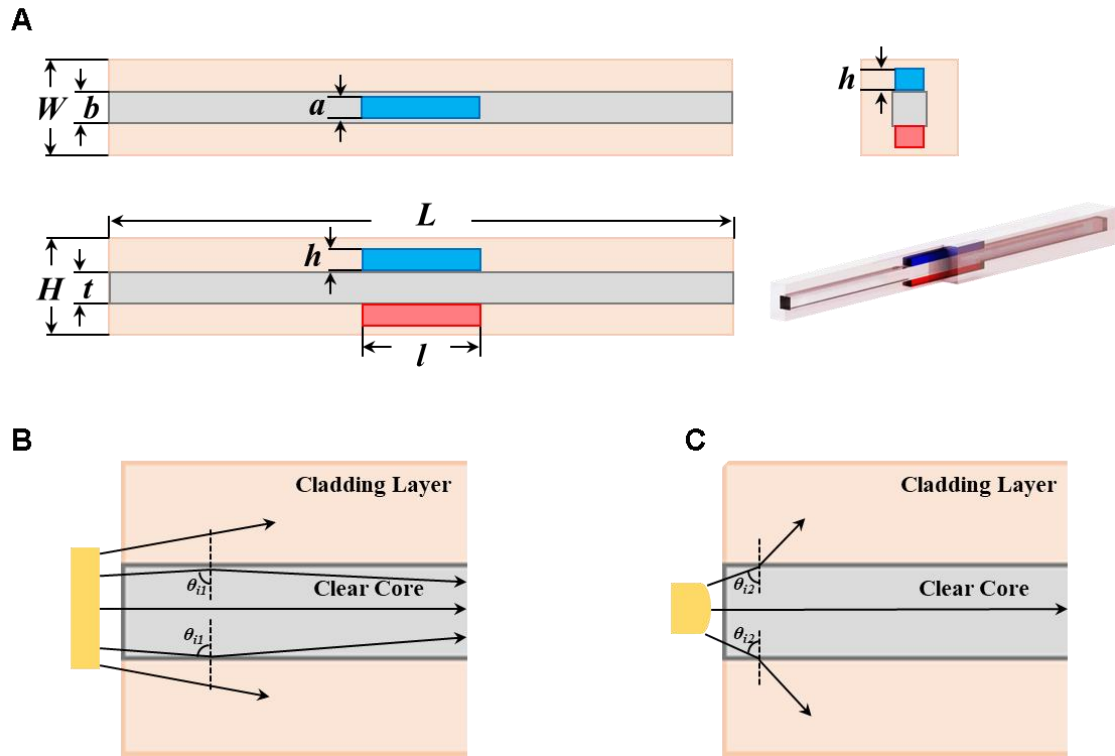
Finally, impact tests were conducted to ascertain the sensitivity to impact and pressure of the three types of the bending sensors. Each sensor was securely affixed to an experimental platform. Pressure of 40 kPa, 80 kPa, and 120 kPa were applied to the sensors individually using a striking device mounted on the standard force sensor (DY-920, DAYSENSOR, China). The results revealed that the non-stretchable bending sensor exhibited robust resilience to impact, maintaining nearly invariant signal output responses. Conversely, the stretchable bending sensor displayed a significant signal response change rate, reaching 21.4%, 42.3%, and 72.3% under 40 kPa, 80 kPa, and 120 kPa impact respectively. Remarkably, the DCLS sensor consistently maintained a signal response change rate within 4%, indicating superior performance compared to the stretchable sensors, albeit slightly inferior to the non-stretchable bending sensors in pressure-unperturbed performance.

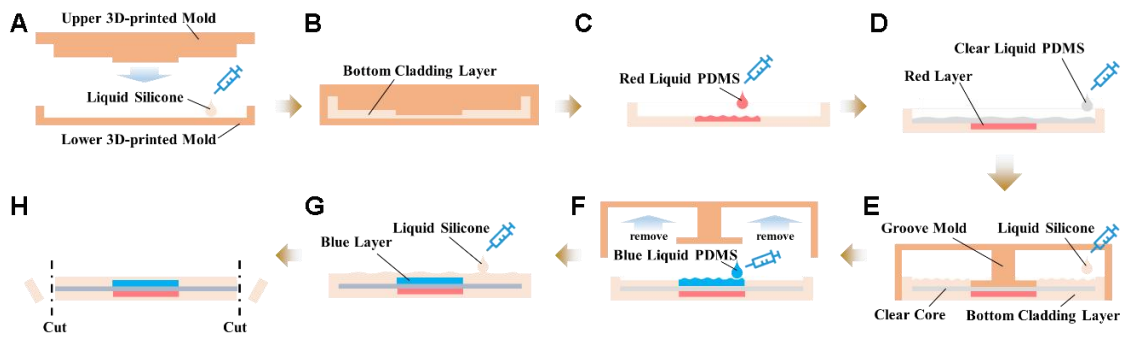**Supplementary Text 6. Design and fabrication of the soft robots**

The soft sorting robot comprises three pneu-nets actuators affixed to a fastener and integrated with a robotic arm (Magician 3, Dobot, China). The DCLS sensor is enclosed within the pneu-nets actuator. The actuators are made of silicone (Ecoflex 00-10, Smooth-On, USA) and interconnected with air tubes. To combine the pneu-nets actuators with the robot arm, the fastener was designed using 3D modeling software (Solidworks 2022, Dassault Systèmes, France) and manufactured utilizing an FDM 3D printer (A8s, JG MAKER, China). To achieve the sorting function of the soft sorting robot, we devised a system architecture encompassing a sorting strategy depicted in Supplementary Figure 11. The system utilizes a microprogrammed control unit (STM32F103RCT6, STMicroelectronics, Italy) to collect sensor data and perform digital filtering preprocessing. The processed data is then transmitted as a data stream to the upper system (PC) via the USART interface. Subsequently, these data undergo automatic sorting strategy processing before being presented to the user. In parallel, a sequence of sorting and grasping commands is dispatched to the robot arm. The master controller of the robot arm conducts inverse kinematics calculations to maneuver its motors, guiding them to the designated sorting positions.

The fish-inspired robot is composed of a fish body, a tail fin, a DCLS sensor, and spine elements. The spine elements and tail fin (made of light-cured resin) were manufactured via the SLA 3D printer (Form3, Formlabs, USA). However, the fish body (made of PLA) was fabricated by the FDM 3D printer (A8s, JG MAKER, China). The DCLS sensor serves as a soft spinal column and is nested inside the spine elements. The fish body is integrated with a microcontroller (Arduino Nano, Italy), a servo motor (KM1850MD, Kingmax, China), a control wheel, and a 3.7 V lithium battery. The microcontroller is used to control the servo motor and process signals from the DCLS sensor. The control wheel, equipped with two tendons, is mounted on the servo motor, enabling the tail fin to swing through tendon-driver methods.
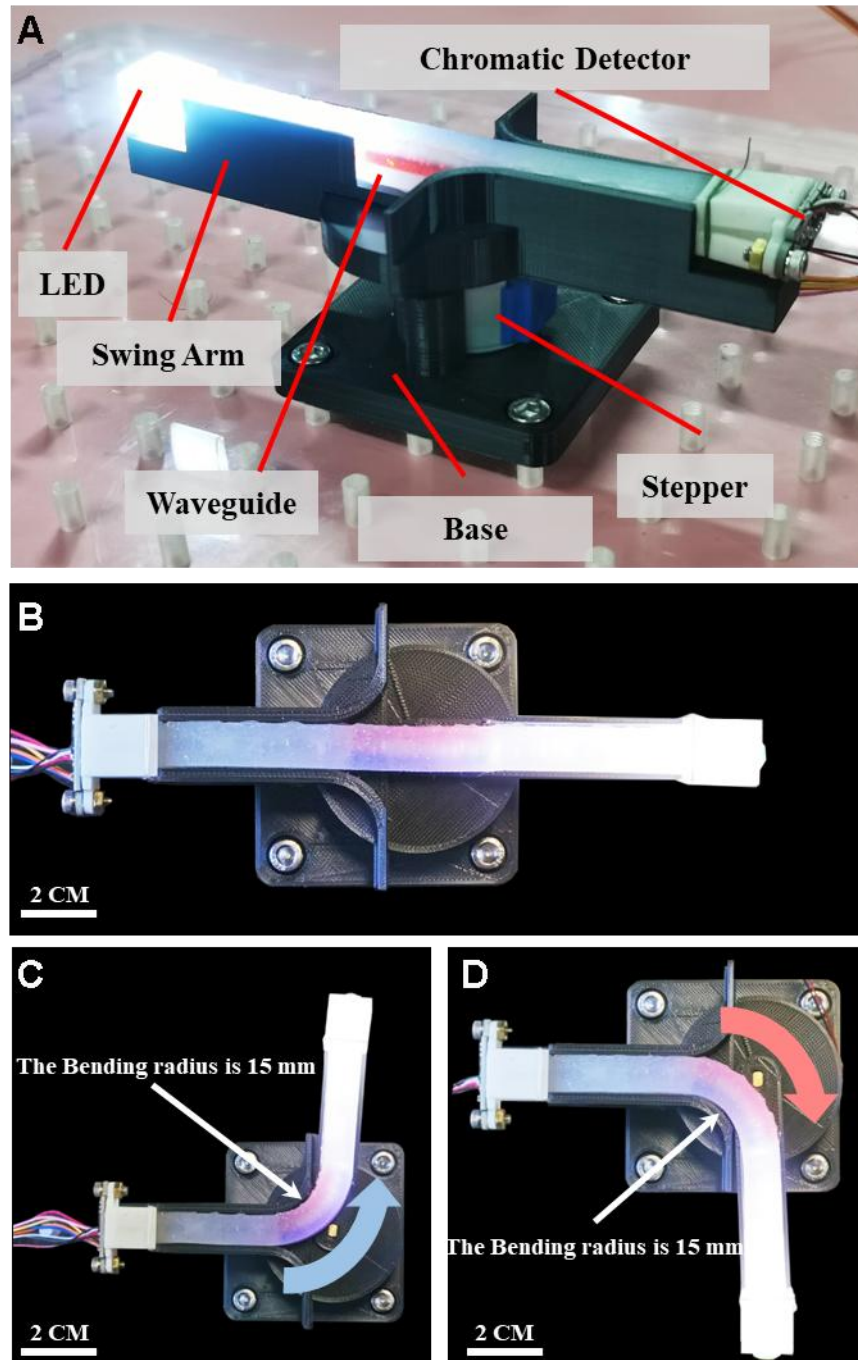
The hand orthotic exoskeleton robot comprises six pneu-nets actuators, five of which facilitate finger flexion and one that aids in wrist flexion. The manufacturing process for these actuators is similar to that of the soft sorting robot. All the actuators are affixed to a hand-like substrate via a silicone adhesive (Sil-Poxy, Smooth-On, USA). The substrate was made of silicone and cured in a hand-like mold. Each actuator of the hand orthotic exoskeleton robot incorporates a DCLS sensor, which is utilized to provide feedback on finger bending angles. The sensor data is transmitted via the IIC bus to a microcontroller (STM32F103RCT6, STMicroelectronics, Italy).
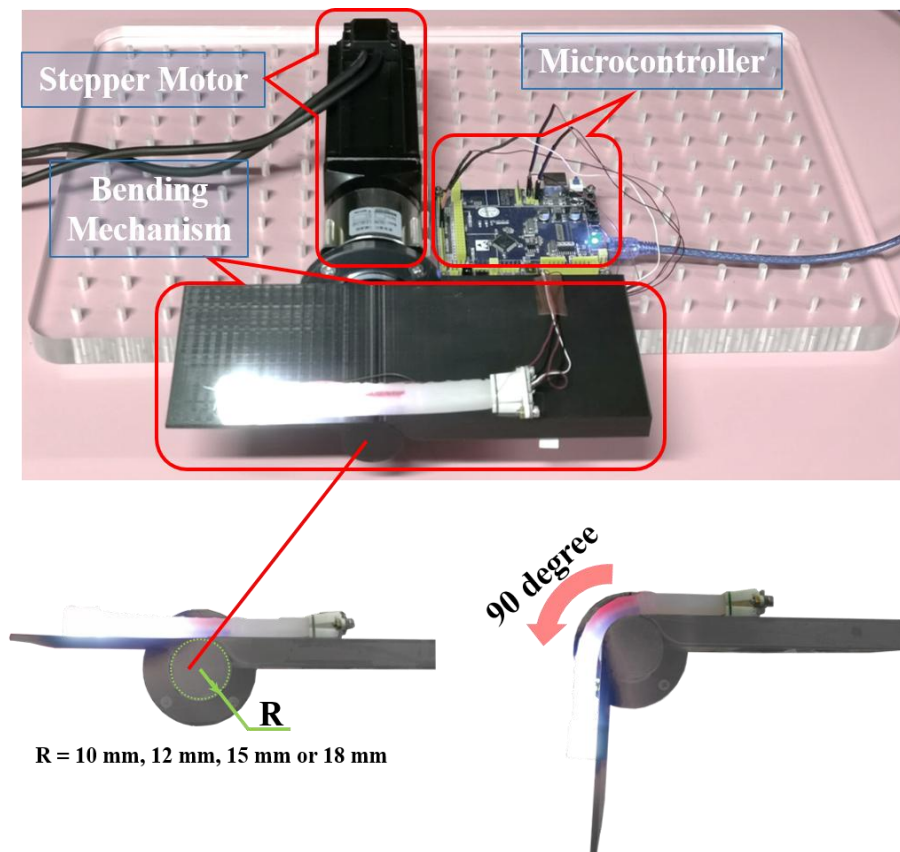
Supplementary Figure 1. Section diagrams of the DCLS sensor and comparing the angle of incidence across different luminous areas. (A) The section diagrams of the DCLS sensor. (B) The angle of incidence for a luminous area larger than the clear core cross-sectional area. (C) The angle of incidence for a luminous area smaller than the clear core cross-sectional area.
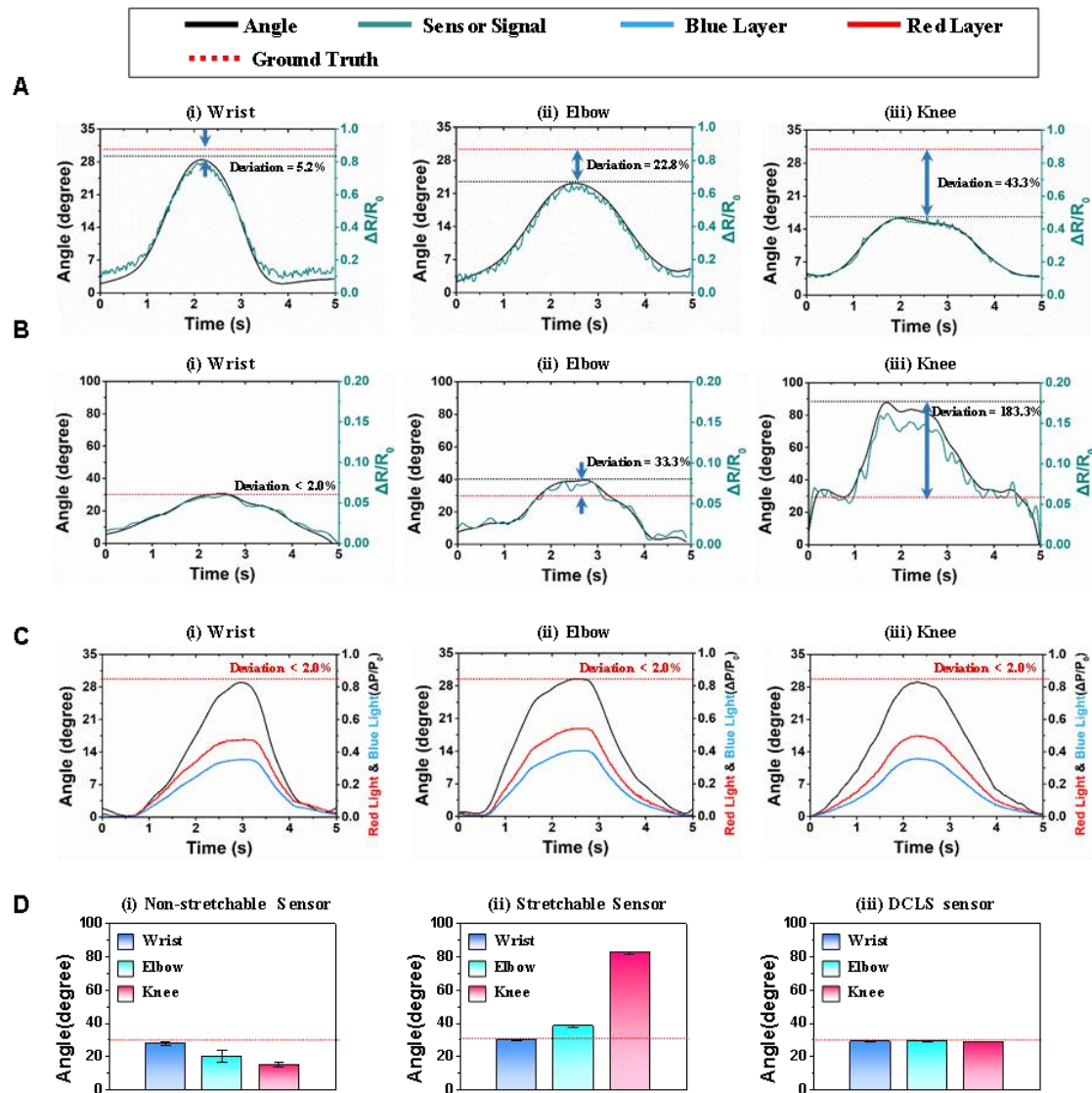
Supplementary Figure 2. Fabrication process of the DCLS sensor. (A) Fabrication of the lower cladding layer using a 3D-printed mold. (B) Curing at 60°C for 3 hours. (C) Injection of red liquid PDMS. (D) Injection of clear liquid PDMS. (E) Cladding casting to seal the clear core. (F) Injection of blue liquid PDMS. (G) Fabrication of the upper cladding layer. (H) Excision of both ends.
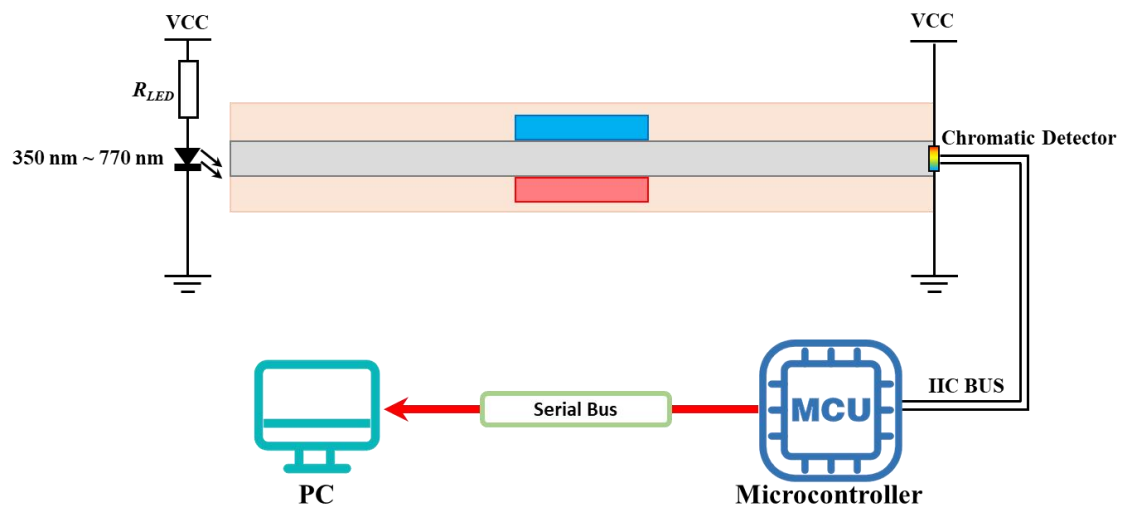
Supplementary Figure 3. (A) Test setup for dual-direction sensing. The swing arm is affixed to the shaft of the stepper, enabling its rotational movement to drive synchronous rotation of the swing arm. The stepper is controlled via the pulse width modulation (PWM) generating by a microcontroller. (B) Primary state. (C) Bending towards the red layer (negative bending). (D) Bending towards the blue layer (positive bending).
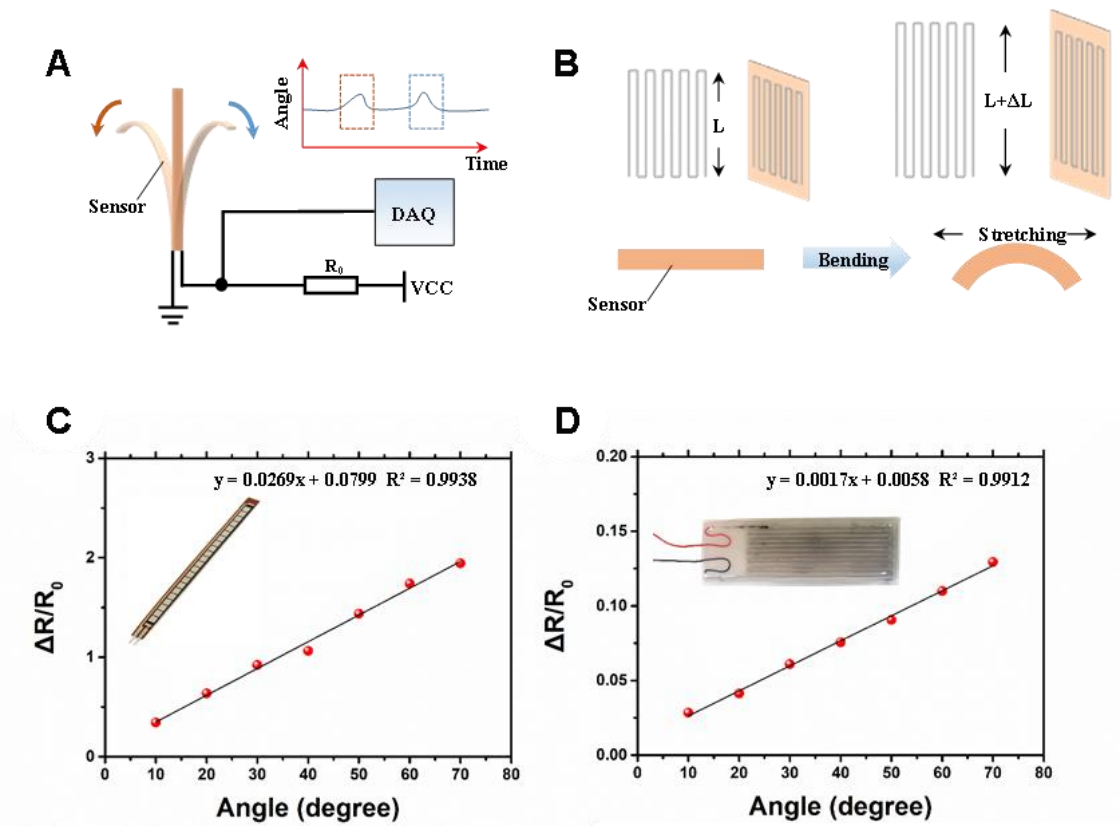
Stepper Motor

Microcontroller

Bending
Mechanism

R

R = 10 mm, 12 mm, 15 mm or 18 mm

90 degree

Supplementary Figure 4. Test apparatus for bending different bending radii and resolution.
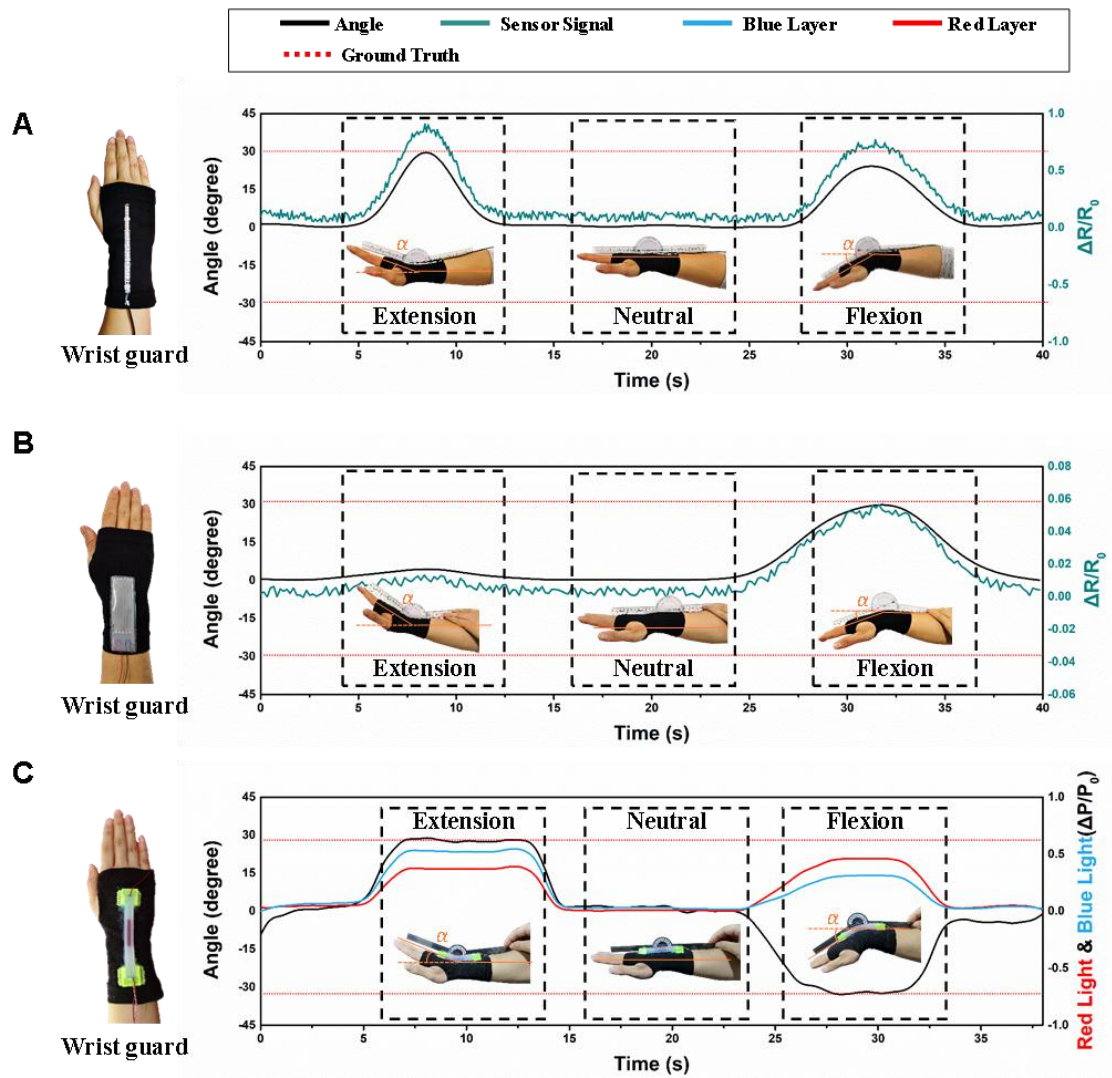
Supplementary Figure 5. Comparison of three types of bending sensors for detecting angle of different human joints. (A-C) Measurement of different human joint angles based on the non-stretchable sensor, stretchable sensor, and the proposed sensor, respectively (Supplementary Movie S1). (D) Comparison of the three types of bending sensors' precision in detecting different human joints.

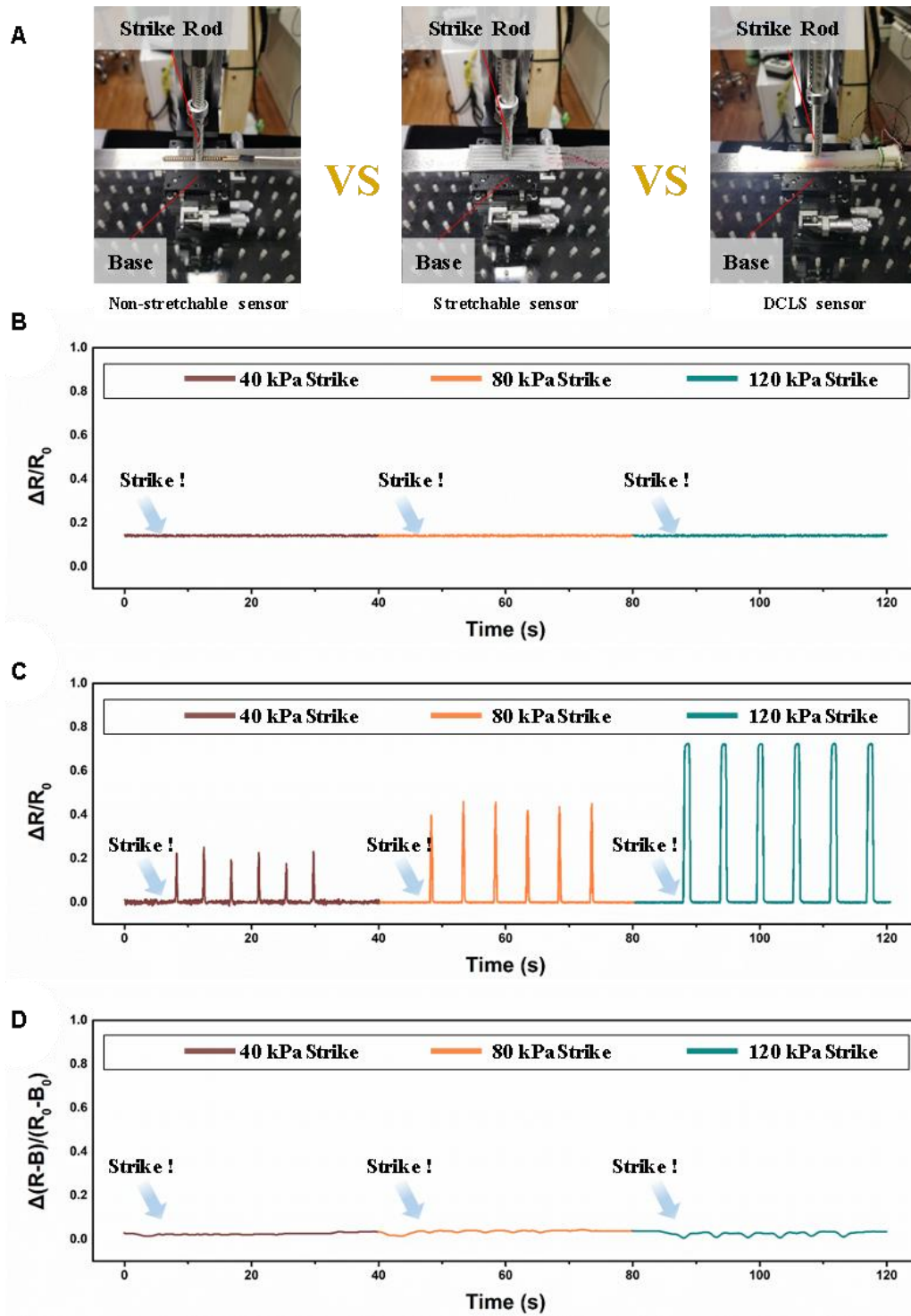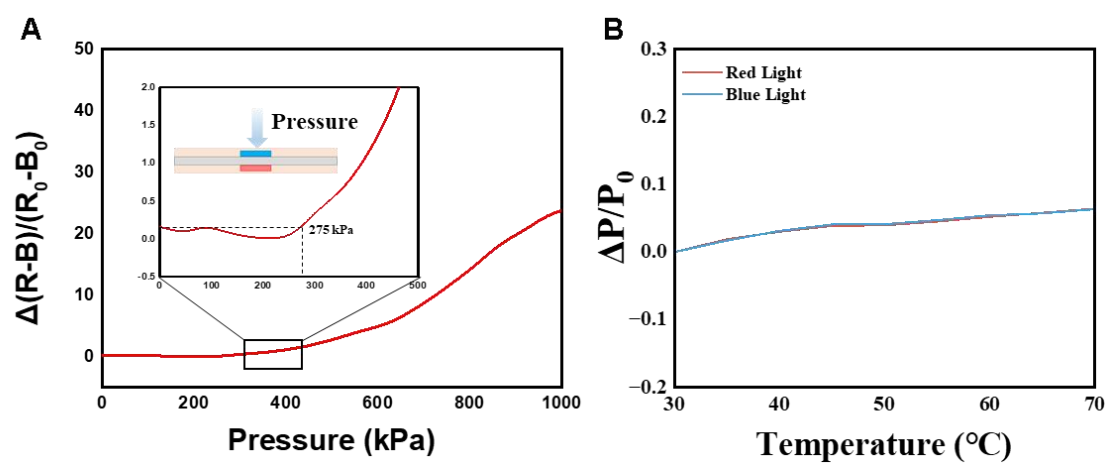**Supplementary Figure 6.** Circuit schematic of the DCLS sensor.

Supplementary Figure 7. Principle and calibration of traditional bending sensors. (A) Principle of the traditional non-stretchable bending sensor. (B) Principle of the traditional stretchable bending sensor. (C) Calibration result of the non-stretchable bending sensor. (D) Calibration result of the stretchable bending sensor.

Supplementary Figure 8. Comparison of three types of bending sensors for discerning different bending directions. (A-C) Measurement of different bending directions based on the non-stretchable sensor, stretchable sensor, and the proposed sensor (Supplementary Movie 2).

Supplementary Figure 9. Signal response comparison of three types of bending sensors under different strikes. (A) Test setup for the three types of bending sensors. (B-D) Output signals of the non-stretchable sensor, stretchable sensor, and proposed sensor under different strikes (Supplementary Movie 3).

Supplementary Figure 10. Durability performance test. (A) mechanical stress limit test. (B) temperature drift test.

Supplementary Figure 11. System architecture of the soft sorting robot.

Supplementary Table 1. Comparative results of the non-stretchable and stretchable bending sensors with the proposed sensor

	Ref	Calibration-free for angle	Calibration-free for bending direction
Non-Stretchable Bending Sensor	[6]	✕	√
	[7]	✕	✕
	[8]	✕	✕
	[9]	✕	✕
	[10]	✕	√
Stretchable Bending Sensor	[11]	✕	✕
	[12]	✕	✕
	[13]	✕	✕
	[14]	✕	✕
	[15]	✕	✕
This work		√	√

Supplementary Table 2. Comparative results of the conventional optical waveguide-based bending sensors with the proposed sensor

	Ref	Size	Pressure-unperturbed properties	Calibration-free
Conventional optical waveguide-based bending sensors	[16]	352 mm (L) × 4 mm (W) × 5 mm (H)	NaN	✖
	[17]	90 mm (L) × 1.5 mm (W) × 1.5 mm (H)	3.0×10^{-4} dB/kPa	✖
	[18]	NaN	2×10^{-3} dB/kPa	✖
	[19]	40 mm (L) × 5mm (Φ)	NaN	✖
	[20]	148 mm (L) x 210mm (W) x 4mm (H)	NaN	✖
	[21]	170 mm (L) x 40mm (W) x 10mm (H)	2.19×10^{-4} dB/kPa	✖
This work		150 mm (L) × 10 mm (W) × 10 mm (H)	1.6×10^{-5} dB/kPa	√

Supplementary Table 3. Variance results of the sensors' signal within hand orthotic exoskeleton robotics in handshaking and knocking state

	Thumb	Index finger	Middle finger	Ring finger	Little finger
Handshaking	1.5×10^{-1}	4.9×10^{-2}	8.5×10^{-4}	8.4×10^{-4}	2.0×10^{-4}
Knocking	2.1×10^{-6}	1.4×10^{-2}	1.5×10^{-2}	2.1×10^{-6}	1.4×10^{-3}

Supplementary Movie 1

Comparison of three types of bending sensors for detecting angle of different human joints.

The video shows the accuracy of three distinct types of bending sensors in measuring angles at wrist, elbow, and knee. The deviation between the sensor measurements and ground truth can be clearly visualized through the computer.

Supplementary Movie 2

Comparison of three types bending sensor for discerning different bending directions.

This video aims to compare the signal response of three distinct types of bending sensors when discerning various bending directions. The non-stretchable sensor (commercial bending sensor), stretchable sensor (liquid metal bending sensor), and the DCLS bending sensor are evaluated in terms of their signal responses during wrist flexion and extension. The video playback speed is set at 2.0×.

Supplementary Movie 3

Signal response comparison of three types of bending sensors under strikes.

In this video, the signal responses of three different bending sensors, namely the non-stretchable sensor (commercial bending sensor), stretchable sensor (liquid metal bending sensor), and the DCLS bending sensor, are compared under different strike forces. Specifically, the sensors are subjected to strikes with forces of 40 kPa, 80 kPa, and 120 kPa, respectively. The video playback speed is set at 3.0×.

Supplementary Movie 4

The DCLS sensor application in a fruit sorting robot.

This video showcases the practical application of the DCLS sensor in a fruit sorting robot. It demonstrates the sorting process of oranges carried out by the robot, which utilizes the DCLS sensor. Real-time sorting results are displayed on the computer interface.

Supplementary Movie 5

The DCLS sensor application in a fish-inspired robot.

The video illustrates the signal response of the DCLS sensor in a fish-inspired robot during its swimming motion. This footage captures how the DCLS sensor detects and responds to the robot's movements.

Supplementary Movie 6

The DCLS sensor application in a hand orthotic exoskeleton robot

This video exhibits the signal response of the DCLS sensor in a hand orthotic exoskeleton robot. It specifically showcases the sensor's performance during activities such as fist clenching, wrist flexion and extension, handshaking, and knocking.

References

1. Planck, M. On the law of distribution of energy in the normal spectrum. *Annalen der physic*. **1901**, *553*, 1.

2. Wang, D., Sheng, B., Peng, L., Huang, Y., & Ni, Z. Flexible and optical fiber sensors composited by graphene and PDMS for motion detection. *Polymers*. **2019**, *11*, 1433. DOI: 10.3390/polym11091433

3. Abro, Z. A., Yi-Fan, Z., Nan-Liang, C., Cheng-Yu, H., Lakho, R. A., & Halepoto, H. A novel flex sensor-based flexible smart garment for monitoring body postures. *Journal of Industrial Textiles*. **2019**, *49*, 262-274. DOI: 10.1177/1528083719832854

4. Wu, Y., Zhou, Y., Asghar, W., Liu, Y., Li, F., Sun, D., ... & Yang, H. Liquid Metal‑Based Strain Sensor with Ultralow Detection Limit for Human‑Machine Interface Applications. *Advanced Intelligent Systems*. **2021**, *3*, 2000235. DOI: 10.1002/aisy.202170073

5. Tao, Y., Han, F., Shi, C., Yang, R., Chen, Y., & Ren, Y. Liquid metal-based flexible and wearable sensor for functional human–machine interface. *Micromachines*. **2022**, *13*, 1429. DOI: 10.3390/mi13091429

6. Hongying, T., Lisheng, H., Xiangrong, W., Huimin, H., Kaili, Z., Juanjuan, W., ... & Huang, J. H. (2022). A Stretchable and Conformable Sensor Fabricated by PVDF Film for human dynamic monitoring. DOI: 10.21203/rs.3.rs-1604483/v1

7. Fu, Q., Fu, J., Zhang, S., Li, X., Guo, J., & Guo, S. Design of intelligent human-computer interaction system for hard of hearing and non-disabled people. *IEEE Sensors Journal*. **2021**, *21*, 23471-23479. DOI: 10.1109/JSEN.2021.3107949

8. Peng, Y., Song, X., Pang, K., Yang, Q., Xu, Z., & Zhang, M. A flexible and stretchable bending sensor based on hydrazine-reduced porous graphene for human motion monitoring. *IEEE Sensors Journal*. **2020**, *20*, 12661-12670. DOI: 10.1109/jsen.2020.3002916

9. Luo, Y., Wang, Z., Wang, J., Xiao, X., Li, Q., Ding, W., & Fu, H. Y. Triboelectric bending sensor based smart glove towards intuitive multi-dimensional human-machine interfaces. *Nano Energy*. **2021**, *89*, 106330. DOI: 10.1016/j.nanoen.2021.106330

10. Li, Z., Hu, F., Chen, Z., Huang, J., Chen, G., Chen, R., ... & Luo, J. Fiber-junction design for directional bending sensors. *npj Flexible Electronics*. 2021, *5*, 4. DOI: s41528-021-00102-2

11. Huang, H., Han, L., Li, J., Fu, X., Wang, Y., Yang, Z., ... & Xu, M. Super-stretchable, elastic and recoverable ionic conductive hydrogel for wireless wearable, stretchable sensor. *Journal of Materials Chemistry A*. **2020**, *8*, 10291-10300. DOI: 10.1039/D0TA02902E

12. Zhou, Z., Chen, K., Li, X., Zhang, S., Wu, Y., Zhou, Y., ... & Chen, J. Sign-to-speech translation using machine-learning-assisted stretchable sensor arrays. *Nature Electronics*. **2020**, *3*, 571-578. DOI: 10.1038/s41928-020-0428-6

13. Gao, Q., Li, H., Zhang, J., Xie, Z., Zhang, J., & Wang, L. Microchannel structural design for a room-temperature liquid metal based super-stretchable sensor. *Scientific reports*. **2019**, *9*, 5908. DOI: 10.1038/s41598-019-42457-7

14. Yang, Z., Li, H., Zhang, L., Lai, X., & Zeng, X. Highly stretchable, transparent and room-temperature self-healable polydimethylsiloxane elastomer for bending sensor. *Journal of colloid and interface science.* **2020**, *570*, 1-10. DOI: 10.1016/j.jcis.2020.02.107

15. Wu, J., Wu, Z., Lu, X., Han, S., Yang, B. R., Gui, X., ... & Liu, C. Ultrastretchable and stable strain sensors based on antifreezing and self-healing ionic organohydrogels for human motion monitoring. *ACS applied materials & interfaces.* **2019**, *11*, 9405-9414. DOI: 10.1021/acsami.8b20267

16. Bai, H., Li, S., Barreiros, J., Tu, Y., Pollock, C. R., & Shepherd, R. F. Stretchable distributed fiber-optic sensors. *Science*. 2020, *370*, 848-852. DOI: 10.1126/science.aba5504

17. Mo, L., Zhang, D., Dou, J., Bai, L., Zhang, Q., & Zhao, X. A High-Performance Optical Waveguide Sensor for Curvature Sensing of Enveloped Soft Actuators. In 2022 IEEE International Conference on Robotics and Biomimetics (*ROBIO, 2022*), 2081-2086).

18. Krauss, H., & Takemura, K. Stretchable optical waveguide sensor capable of two-degree-of-freedom strain sensing mediated by a semidivided optical core. IEEE/ASME Transactions on Mechatronics. **2022**, *27*, 2151-2157. DOI: 10.1109/TMECH.2022.3175205

19. Del Bono, V., McCandless, M., Wise, F. J., & Russo, S. A soft miniaturized continuum robot with 3D shape sensing via functionalized soft optical waveguides. In 2024 IEEE International Conference on Robotics and Automation (*ICRA, 2024*), 5309-5316.

20. Mak, C. H., Li, Y., Wang, K., Wu, M., Ho, J. D. L., Dou, Q., ... & Kwok, K. W. Intelligent Shape Decoding of a Soft Optical Waveguide Sensor. *Advanced Intelligent Systems*. **2024**, *6*, 2300082. DOI: 10.1002/aisy.202300082

21. Hassan, A., Aljaber, F., Vitanov, I., & Althoefer, K. Performance Evaluation and Optimisation of Multi-point Waveguide based optical Sensor for Soft Robots. In 2022 IEEE International Conference on Flexible and Printable Sensors and Systems (*FLEPS, 2022*), 1-4.